



Delft University of Technology

## Evaluating compressive mechanical LDPM parameters based on an upscaled multiscale approach

Lifshitz Sherzer, G.; Schlangen, E.; Ye, G.; Gal, A. E.

**DOI**

[10.1016/j.conbuildmat.2020.118912](https://doi.org/10.1016/j.conbuildmat.2020.118912)

**Publication date**

2020

**Document Version**

Final published version

**Published in**

Construction and Building Materials

**Citation (APA)**

Lifshitz Sherzer, G., Schlangen, E., Ye, G., & Gal, A. E. (2020). Evaluating compressive mechanical LDPM parameters based on an upscaled multiscale approach. *Construction and Building Materials*, 251, Article 118912. <https://doi.org/10.1016/j.conbuildmat.2020.118912>

**Important note**

To cite this publication, please use the final published version (if applicable).

Please check the document version above.

**Copyright**

Other than for strictly personal use, it is not permitted to download, forward or distribute the text or part of it, without the consent of the author(s) and/or copyright holder(s), unless the work is under an open content license such as Creative Commons.

**Takedown policy**

Please contact us and provide details if you believe this document breaches copyrights.

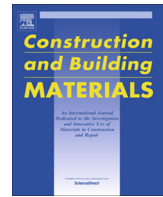
We will remove access to the work immediately and investigate your claim.

***Green Open Access added to TU Delft Institutional Repository***

***'You share, we take care!' – Taverne project***

***<https://www.openaccess.nl/en/you-share-we-take-care>***

Otherwise as indicated in the copyright section: the publisher is the copyright holder of this work and the author uses the Dutch legislation to make this work public.



## Evaluating compressive mechanical LDPM parameters based on an upscaled multiscale approach



G. Lifshitz Sherzer<sup>a</sup>, E. Schlangen<sup>b</sup>, G. Ye<sup>b</sup>, A.E. Gal<sup>a,\*</sup>

<sup>a</sup> Department of Structural Engineering, Ben-Gurion University of the Negev, Beer-Sheva, Israel

<sup>b</sup> Microlab, Section of Materials and Environment, Faculty of Engineering and Geoscience, Delft University of Technology, Delft, Netherlands

### ARTICLE INFO

#### Article history:

Received 8 July 2019

Received in revised form 19 March 2020

Accepted 25 March 2020

#### Keywords:

Fracture of concrete

Multiscale modelling

Lattice model

Upscaling procedure

Pore collapse

### ABSTRACT

We propose an upscaled methodology for evaluating the compressive parameters of the Lattice Discrete Particle Model (LDPM) for a multiscale analysis of concrete structures. This methodology is based on mechanical and chemical models on a wide range of concrete scales. We show that the compressive mechanical parameters are related mainly to material compaction that occurs at the scale of cement paste, the scale containing porosity properties. Therefore, these compressive LDPM parameters are subsequently evaluated based on chemical and mechanical simulations at the cement paste level. Finally, the suggested methodology was verified and validated.

© 2020 Elsevier Ltd. All rights reserved.

## 1. Introduction

The behavior of highly confined concrete is of great significance to engineering issues, including microstructure and mechanical properties, the material design of the anchorage of pre-stressing reinforcement, containment vessels, bridge pillars, and columns in high-rise buildings; and the behavior of individual, unique concrete structures exposed to projectile impact. Here we focus on compressive strength under high levels of confinement and evaluate the pore collapse and material compaction parameters for the Lattice Discrete Particle Model (LDPM), in contrast to the work of [1] which used an experimental method to evaluate these same parameters. In the three decades since the pioneering work of Balmer [2], much research has been devoted to the study of the confined behavior of concrete [3–11].

If a material is capable of permanent volume change, then it contains voids. Compaction of concrete is the physical collapse of its porous microstructure at the initial peak point. As stresses continue to increase beyond this point, a hardening behavior in the stress-strain curve occurs due to the closure of pores. To provide a better understanding of the hydrostatic behavior of concrete, [12] performed an optical observation. This observation clearly revealed a closure of macroscopic porosity along with damage at the cement matrix/aggregate interface, known as the Interfacial

Transition Zone (ITZ) or “transition aureole.” In another study, [13] focused on the effects of the water/cement (w/c) ratio of fresh concrete composition on hardened concrete behavior under very high confinement, finding that a drop in w/c ratio pushes the confinement threshold higher. Furthermore, Marino [14] studied experimental and analytical relationships to enable prediction of entire stress-strain curves for confined high-strength concrete under compression. The conclusion drawn was that, as degree of confinement increased, the compressive strength at the initial yielding point and the ductility of high strength concrete core specimens confined by rectilinear steel ties both increased. However, this rate of increase was lower than that of normal strength concrete with similar confinement degrees. The analytical model developed to predict the compressive stress-strain of confined high strength concrete core produced a stable fit with experimental results.

The various scales and the applied models used in the current methodology are presented in Fig. 1. The cement paste scale unit cell (100 μm) consists of cement particles with dimensions ranging from 1 μm to 50 μm; these particles include solids, namely, unhydrated cement, inner product, outer product, interface layers, and capillary pores containing liquid water and water vapor. In order for the chemical simulation to achieve the microstructure of cement paste, we used the HYMOSTRUC3D model [15,16]. Likewise, to simulate the mechanical properties of the cement paste scale, lattice models were used [17] rather than other micromechanical models [18,19]. The mortar-s scale unit cell

\* Corresponding author.

E-mail address: [gili.lifshitz@gmail.com](mailto:gili.lifshitz@gmail.com) (A.E. Gal).

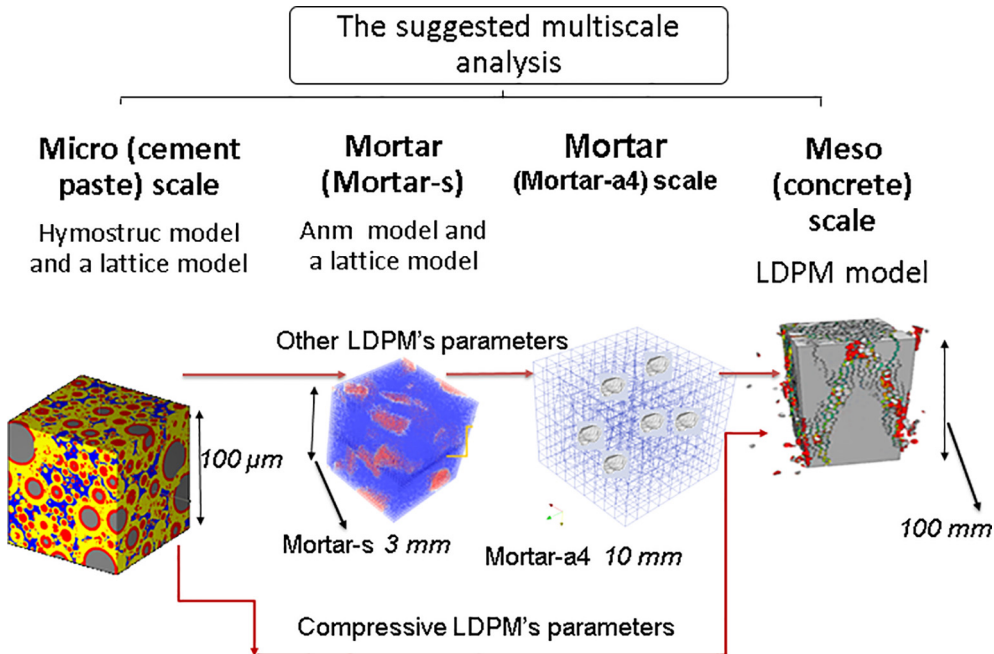


**Fig. 1.** The different scales comprising multiscale methodology.

(3 mm) consists of sand particles; with dimensions ranging from 0.5 mm to 1.2 mm, these solid particles are embedded in the cement paste matrix, including in the ITZs. For the aggregate distribution of mortar-s, the Anm model [20] was applied, while for the mechanical properties, the lattice model [17] was applied. The mortar-a4 scale unit cell (10 mm) consists of aggregates with dimensions ranging from 2.36 mm to 4 mm embedded in a matrix of mortar-s, with the fine aggregates surrounded by an ITZ. For this scale, the same Anm and lattice models were applied. The characterization of mortar-a4 was selected to highlight the fact that the smallest aggregate size of the concrete is 4 mm. The concrete scale, considered as a two-phase composite material consisting of coarse aggregates greater than 4 mm and up to 14 mm, was embedded in a matrix of mortar-a4. These coarse aggregates were also embedded in an ITZ; in this sense, the material concrete-scale is better considered as a three-phase composite. However, the third phase, consisting of the ITZ, was taken into account through the failure of mortar-a4. For this scale the LDPM was applied. Finally, the structure scale, often considered as the engineering scale on which concrete is treated as a homogeneous continuum, was not addressed in this study.

Evaluating the compressive LDPM parameters, dealt with by this paper, does not require the analysis of sand and mortar a4 scales. Since concrete porosity is represented only at the cement paste scale, these results were directly upscaled to the mortar-a4 scale to obtain the LDPM compressive parameters, as illustrated in Fig. 1.

Lastly, a comparison between High Friction (HF) and Low Friction (LF) uniaxial compression experimental results and LDPM numerical simulations based on the proposed upscaled parameters were used for the validation process.

## 2. Objectives of this research

The aim of this research is to introduce algorithms and procedures for predicting multi-scale behavior of concrete due to its components. To achieve these goals, we conducted two type sets of simulations: 1) of material structure and 2) of mechanical per-

formance. The tools served for these goals are: For material structure modeling HYMOSTRUC3D (cement paste) and the Anm (mortar-s and mortar-a4), and the mechanical models are the lattice (cement paste, mortar-s and mortar-a4) and LDPM (concrete). LDPM combines the structural and mechanical modeling together.

The developed method combines the two models by exchanging parameters representing the mechanism of failure in different scales.

Fig. 2 represent a flow chart developed for the exchange and passing parameters. The chart begins first by chemical simulation of the cement paste as well as formation of different phases due to the chemical reaction between the cement paste and water. Consequently, the microstructure of the model is evaluated; the results are then used for two purposes: 1) the evaluation of compressive strength parameters and 2) the evaluation of tension and shear parameters. For the first aim the evaluated parameters are directly transferred from the cement paste to the concrete (LDPM) scale. For the second aim the parameters are first upscaled to mortar-s scale, then to mortar-a4 scale and finally to the concrete scale (LDPM).

As shown in Fig. 2, on the mechanical properties for the lattice for the first aim the mechanism of the pore collapse is evaluated from hydrostatic and uniaxial confined test, while for the second aim the mechanism of fracturing, shearing, and elastic behavior are obtained from the upscaled mortar-a4 shear and tensional test.

## 3. Methodology

Compressive LDPM parameters were retrieved from simulations of different confinement conditions at the cement paste scales. This methodology differs from that previously suggested [21] for use in evaluating elastic shear and fracture LDPM parameters retrieved from simulations at the mortar-a4 scale. These two methodologies are based on evaluating LDPM parameters using a mechanical lattice model by analyzing cement-paste/mortar-a4 specimens under different load combinations [22,23]. The interaction between neighboring particles of LDPM elements is governed by a constitutive law applied on the facet (i.e., the boundary

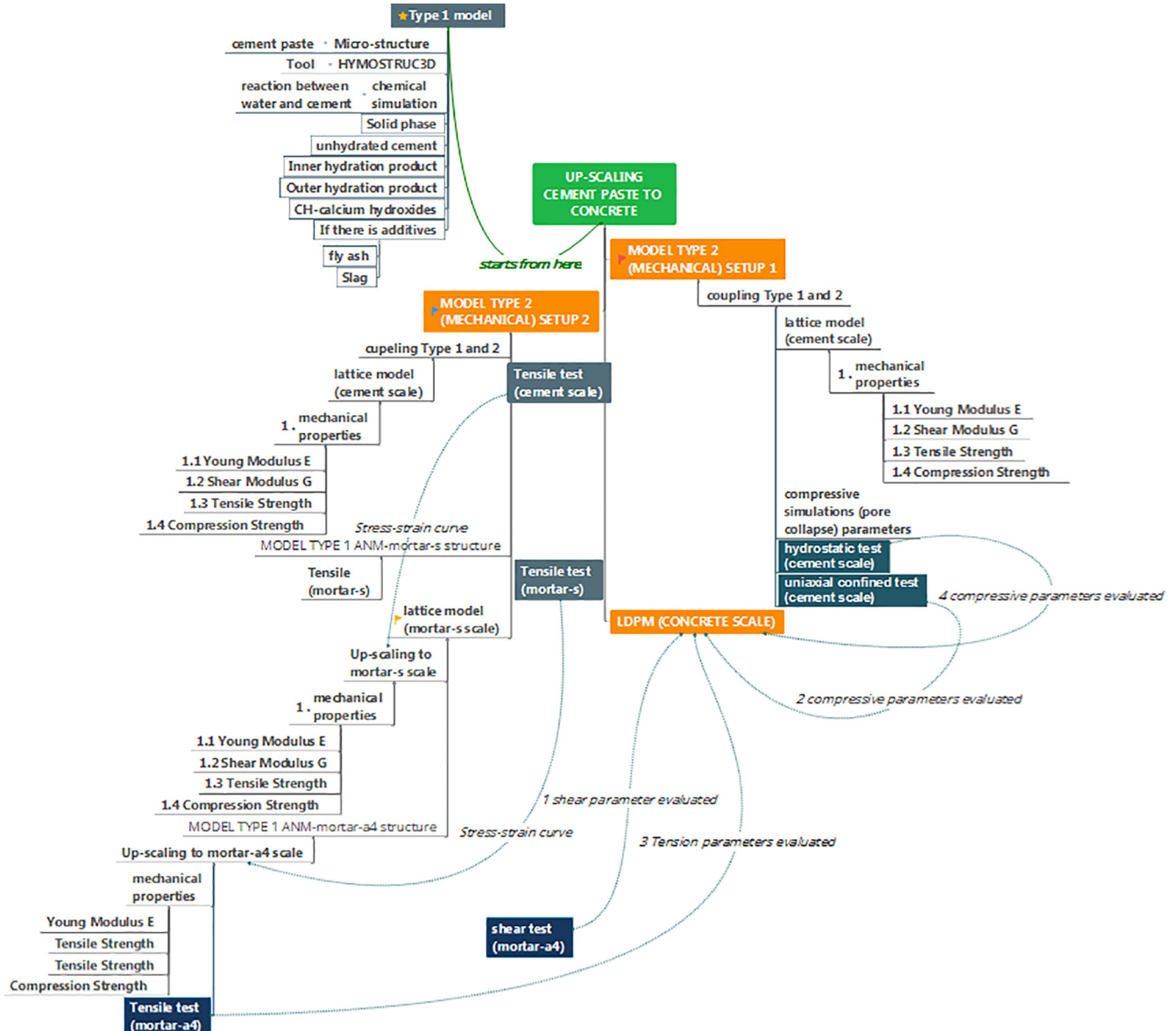


Fig. 2. The flow chart for the exchange and passing parameters.

between two elements), whereby an element characterized by the aggregate is bonded together with mortar. The facet is located in the mortar region, therefore the mortar-a4 unit cell is appropriate for representing failure mechanisms for the LDPM elastic, shear, and fracture constitutive laws [21]. However, in order to represent the failure criterion of the pore collapse mode, a scale that contains porosity should be considered. Consequently, a unit cell of the cement paste was chosen for this role, since it is the only scale included in the suggested methodology that includes porosity. In other words, in our upscaling procedure the impact of the pore collapse phenomenon can be captured numerically only at the cement paste scale. Fig. 3 presents the passing flow information we advocate to evaluate the parameters of different failure modes.

The computational framework of the methodology we propose is schematically demonstrated in Fig. 4. This process begins with a chemical simulation, where the data required for the HYMOS-TRUC3D model [15,16], chosen to obtain the microstructure, are the mineralogical and chemical compositions of the cement paste as well as hydration rate parameters. The process continues with

a numerical simulation performed on the cement paste by the lattice model (see [17], which requires the microstructure and mechanical properties of each phase. In the current work this lattice model simulation fulfilled two purposes. The first purpose was to simulate two numerical compressive tests under hydrostatic and confined uniaxial compression loads with the objective, due to pore collapse, of evaluating the compressive parameters of the LDPM [22,23]. The second purpose was to simulate the numerical tension test in order to evaluate other mechanical properties of these LDPM parameters. The second process was followed by a numerical tensile test on the mortar-s unit cell for the evaluation of the mechanical properties of the matrix at the upper scale. In a previous study [21] two simulations tests (i.e., tension and pure shear) of the mortar-a4 unit cell were performed to evaluate the elastic, fracture, and shear parameters of the LDPM [22,23].

While the upscaling of the five other parameters associated with elastic, fracture, and shear response, have been previously evaluated [21], here we present the successful upscaling method of the six compressive LDPM parameters from the lower scale that are related to the pore collapse and material compaction modes. A

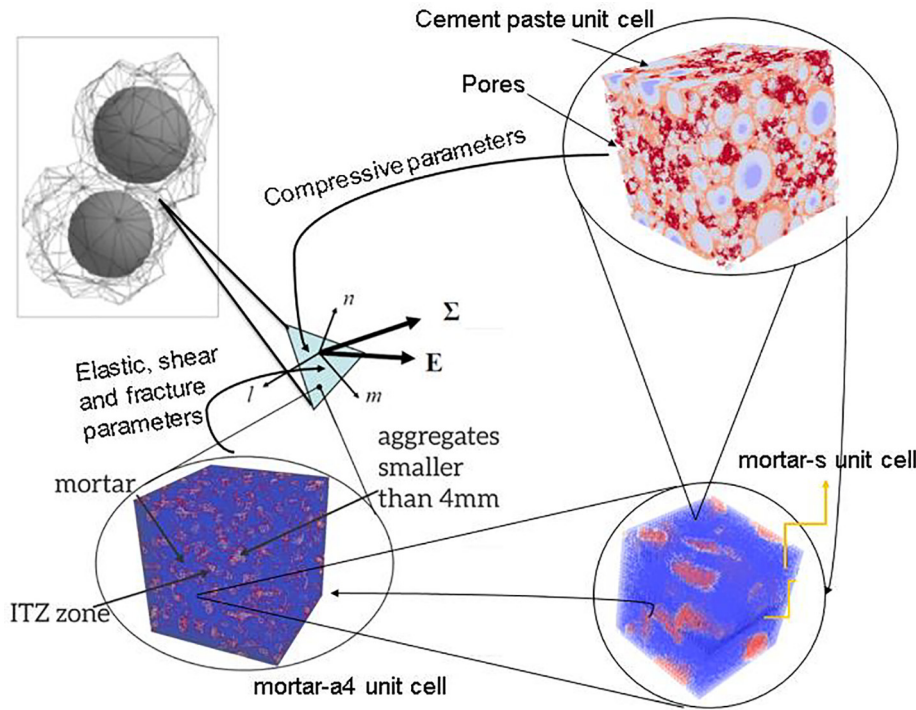


**Fig. 3.** Information passing flow of proposed upscaling methodology.

detailed explanation of how these models function is presented below.

#### Lattice simulation

The lattice model, represented by the discretization of the continuum material together with a network of lattice elements characterized by Timoshenko beam elements [17], simulates the material response under different types of loads. Additionally, the beam coordinate system contains the longitudinal  $x$  axis at the center, and the  $y$  and  $z$  axes in the lateral directions. A beam element has two nodes, each of which has six degrees of freedom: three spatial displacements and three rotation components, as presented in Fig. 5.

The relationship between the strains and displacements is represented by the kinematic equation, as shown in Eq. (1):

$$\varepsilon_x(x) = \frac{du(x)}{dx} \quad (1)$$

The equilibrium equation is presented in Eq. (2)

$$A \frac{d\sigma_x(x)}{dx} + f(x) = 0 \quad (2)$$

where  $A$ , as the cross-section area of the element  $f(x)$ , is the external axial force, while  $\sigma_x(x)$ ,  $\varepsilon_x(x)$  and  $u_x(x)$  are the stress, strain, and displacements, respectively.

The relationship between stresses and strains is represented by a constitutive equation, that relates between the bending moment  $m(x)$  that changes over  $x$  axis to the curvature, as seen in Eq. (3)

$$m(x) = -EI_z \cdot \frac{d\theta(x)}{dx} \quad (3)$$

where  $\theta(x)$  is the rotational displacement,  $E$  is the axial elastic modulus and  $I_z$  is the moment of inertia about the  $z$  axis.

The stress induced in the beam elements is then calculated; when a beam element passes the comparative strength as presented in Eq. (4), it is removed from the lattice network. This process repeats itself until all elements fail. This beam removal approach is based on the brittle fracture law [24] grounded on

the maximum stress that occurs in the outermost fiber of a beam element as a result of the moment and normal force in the beam, as depicted in Eq. (4):

$$\sigma = \alpha_N \frac{F}{A} + \alpha_M \frac{(M_{xOy}, M_{xOz})}{W} \quad (4)$$

where  $A$  is the area of the cross-section,  $W$  is the section modulus,  $\alpha_N$  and  $\alpha_M$  are the “normal force influence factor and the bending influence factor,” for which the chosen values are 1.0 and 0.05, respectively [see also [25]].

#### 3.1. Meso-structure parameters

The meso-structure consists of cement content ( $c$ ), aggregate-to-cement ratio ( $a/c$ ), water-to-cement ratio ( $w/c$ ), maximum aggregate size ( $d_a$ ), minimum aggregate size ( $d_0$ ), and granulometric distribution (Fuller curve) coefficient ( $n_F$ ). The Fuller coefficient can be defined using a curve fitting between the sieve analysis and the granulometric distribution function of Fuller.

#### 3.2. Evaluating mechanical parameters of LDPM model

LDPM kinematics affected by rotations and displacements between neighbors’ aggregates provide the strain vector. Constitutive law is dependent upon the ratio between the strain vector and the stress vector at each facet; variables of this law are derived from fifteen mechanical parameters. (For more details see [22]. These parameters, which each has a physical meaning represented by a different failure mode, are located on the facet in the mortar region and thus can be named “microplane parameters.” The proposed upscaling method evaluates these parameters by applying different combinations of loads on the cement/mortar-a4 unit cells; in this way the LDPM’s constitutive law is controlled by this failure phenomena. The following Section 3.2.4 present LDPM field equations and their required mechanical parameters; for details see [22].

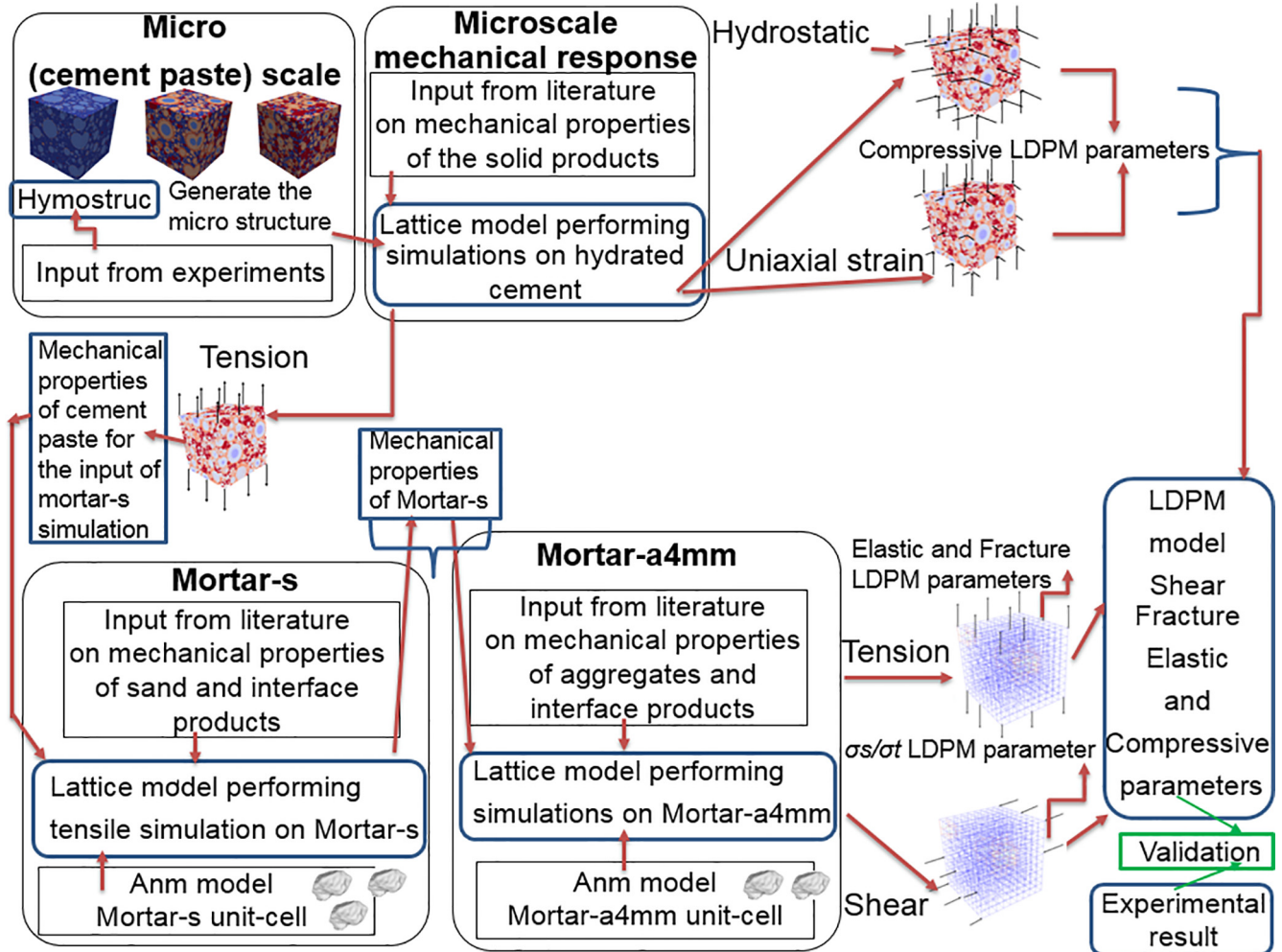


Fig. 4. Computational framework of suggested upscaling methodology.

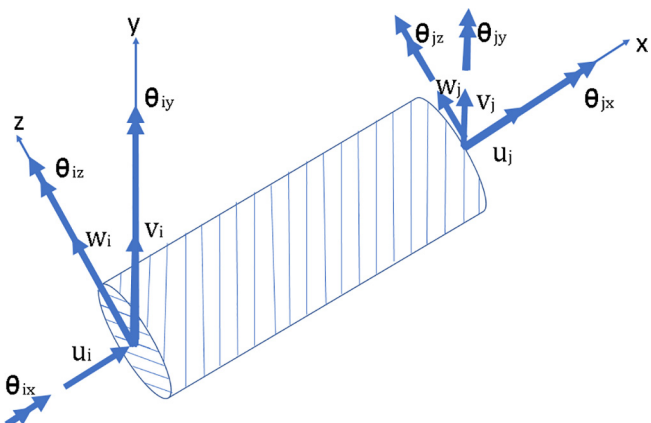


Fig. 5. A Timoshenko beam element in the lattice model [17]

### 3.2.1. LDPM kinematics based on microplane model

Microplane theory can be divided into a three-step procedure, as follows. The first step is to apply the kinematics by calculating the relative displacements (and rotations) of adjacent nodes, or particles, in each facet, as represented in Eq. (5)

$$u(x) = u_i + \theta_i \times (x - x_i) \quad (5)$$

where  $x$  is located at the centroid point,  $u_i$  is the displacement, and  $\theta_i$  is the rotational degrees of freedom of node  $i$ .

Strain vectors are then macroscopically calculated from the displacements and element lengths from which the strain tensors are projected; the assumption is that the projected macroscopic strain tensor is equivalent to microplane strain. This determined strain is then decomposed into normal and two-shear components.

The second step is to apply the constitutive law on the microplane level; constitutive equations are controlled from strain vectors and stress. It should be noted that constitutive law is calculated differently for elastic and inelastic behaviors.

#### 3.2.2. LDPM elastic constitutive law

Elastic parameters are characterized by their material properties and derived from Eqs. (10) and (11), whose relations are evaluated by the “kinematically constrained homogenization of a random assemblage of the rigid spherical particles of various sizes interacting through elastic contacts” [22]. These equations can estimate elastic parameters, depending on macroscopic experiments monitored for obtaining Young’s modulus and Poisson’s ratio.

#### 3.2.3. LDPM inelastic constitutive laws

The equations contained here predict the non-linear and inelastic parts of constitutive law, characterized by three different physical mechanisms of mesoscale behavior, as detailed below:

**3.2.3.1. LDPM fracturing and cohesive behavior.** Cohesive behavior characterizes the interaction between shear and tension failures, as presented in Eq. (6)

$$\sigma_{bt}(\varepsilon, \omega) = \sigma_0(\omega) \exp\left[-H_0(\omega) \frac{\langle \varepsilon_{max} - \varepsilon_0(\omega) \rangle}{\sigma_0(\omega)}\right] \quad (6)$$

where  $\sigma_{c0}$  is the yielding compressive stress,  $\omega$  represents the degree of failure between shear and tension,  $H_0$  is the hardening Young's modulus, brackets  $\langle \cdot \rangle$  are used in the Macaulay sense, i.e.,  $\langle x \rangle = \max(x, 0)$ , and  $\varepsilon_0$  and  $\varepsilon_{max}$  are, respectively, the strain at the yielding point and the maximum strain during the loading history.

**3.2.3.2. LDPM pore collapse and material compaction.** Inelastic behavior characterizes concrete under high compressive hydrostatic loads, under which there is an initial pick point due to pore collapse, followed by a re-hardening behavior effected from the closure of the pores that leads to densification of the concrete. These different phases are calculated as follows:

$$\sigma_{bc}(\varepsilon_D, \varepsilon_V) = \begin{cases} \sigma_0 + \langle -\varepsilon_V - \varepsilon_{c0} \rangle H_c(r_{DV}) & \text{for } -\varepsilon_V \leq \varepsilon_{c1} \\ \sigma_{c1}(r_{DV}) \exp\left[\frac{\langle -\varepsilon_V - \varepsilon_{c1} \rangle H_c(r_{DV})}{\sigma_{c1}(r_{DV})}\right] & \text{otherwise} \end{cases} \quad (7)$$

where  $H_c$  is the initial hardening modulus and  $\varepsilon_1$  is the volumetric strain at the beginning of the hardening  $\sigma_{c1}(r_{DV}) = \sigma_{c0} + (\varepsilon_1 - \varepsilon_{c0}) H_c(r_{DV})$ .

**3.2.3.3. Frictional behavior.** Under compression stress, shear stress is developed due to the effect of friction, computed using classical incremental plasticity:

$$\sigma_{bs}(\sigma_N) = \sigma_s + (\mu_0 + \mu_\infty) \sigma_{N0} - \mu_\infty \cdot \sigma_N - (\mu_0 - \mu_\infty) \sigma_{N0} \exp(\sigma_N / \sigma_{N0}) \quad (8)$$

where  $\sigma_s$  is cohesive stress,  $\mu_0$  is the initial internal friction coefficient,  $\mu_\infty$  is the internal asymptotic friction coefficient, and  $\sigma_{N0}$  is the transitional stress.

#### 3.2.4. LDPM global equilibrium equations

At this step, overall macroscopic response from the material's mechanical parameters located on the facet is calculated. This response is represented by the homogenization process, controlled by the Principle of Virtual Work (PVW)" [22]; the internal work is calculated from equilibrium, as can be seen in Eq. (9)

$$\delta W_k = l_e A_k \sigma_k^T \delta \varepsilon_k \quad (9)$$

where  $A_k$  is the area of the projected facet,  $\sigma_k$  is the transposed stress vector summed up at the facet,  $\varepsilon_k$  is the strain vector summed up at the facets, and  $l_e$  is the element length.

#### 3.2.5. Mechanical LDPM parameters

For the sake of convenience, constitutive law parameters have been separated into the following groups: elastic, tensile, pore collapse and material compaction, friction, and fracture (see also [22] (Cusatis, Pelessone, et al., 2011).

**3.2.5.1. Elastic parameters.** This group is characterized by two elastic parameters:

- (1)  $E_0$  is the normal elastic modulus (i.e., stiffness of the normal facet behavior), presented in Eq. (10), which governs LDPM response in the elastic mode of operation

$$E_0 = \frac{1}{1 - 2\nu} E \quad (10)$$

where  $E$  is the macroscopic elastic parameter; this result is obtained by the experimental test.

- (2)  $\alpha$  is the shear-normal coupling parameter represented in Eq. (11)

$$\alpha = \frac{1 - 4\nu}{1 + \nu} \quad (11)$$

where  $\nu$  is the assumed Poisson's ratio parameter of concrete; this result is obtained by the experimental test.

**3.2.5.2. Fracture parameters.** This group is characterized by two parameters, representing normal displacement at the facet between neighbors' particles, or aggregates, as well as providing the tensile mechanism. The definition of these parameters is as follow:

- (3)  $\sigma_t$ , tensile strength; and
- (4)  $l_t$ , modified characteristic length for concrete using the LDPM (see [22,26], as described in Eq. (12)).

$$l_t = \frac{2E_0 G_t}{\sigma_t^2} \quad (12)$$

Tensile strength and fracture energy were retrieved using a uniaxial tension simulation at the mortar-a4 scale, as documented in [21].

**3.2.5.3. Pore collapse under compaction.** This group contains six parameters representing a pore collapse and material compaction behavior:

- (5)  $\sigma_{c0}$  is the yielding compressive stress that defines the behavior of facet normal displacement under compression;
- (6)  $E_d/E_0$  is the densification ratio, where  $E_d$  densifies the normal modulus
- (7)  $H_{c0}/E_0$  is the initial hardening modulus ratio
- (8)  $k_{c0}$  is the transitional strain ratio that governs the volumetric strain at which the concrete starts to re-harden due to material densification
- (9)  $k_{c1}$  governs the nonlinear evolution of the normal facet stress in compression, which represents the deviatoric strain threshold ratio; and
- (10)  $k_{c2}$  governs the nonlinear evolution of the normal facet stress in compression, which represents the deviatoric damage parameter.

An effort was made to obtain this group of parameters from a hydrostatic compression numerical test and a uniaxial confined numerical test on the cement paste scale. In these simulations specimens were loaded under compression from all directions (hydrostatic), and were loaded under compression in the longitudinal direction at the same time that the transverse direction was confined (see Fig. 6a and c, respectively).

The following six parameters have been upscaled from a hydrostatic compression cement paste simulation resulting in an  $r_{DV}$  deviatoric-to-volumetric strain ratio equal to zero.  $r_{DV}$  equal to zero is suitable for the equation shown in Fig. 4b by [22] as a continuous black line; this simulation test was thus chosen to represent the following criteria parameters of four LDPMs' failure caused by pore collapse. These four parameters are evaluated as the yielding compressive stress at the initial peak value in the stress-strain curve; here  $E_d$  assumed as  $E_0$ ; the hardening Young's modulus ( $H_0$ ) acquired from the hardening slope of the stress-strain curve; and the material parameter governing the start of re-hardening ( $K_{c0}$ ) evaluated from Eq. (13)

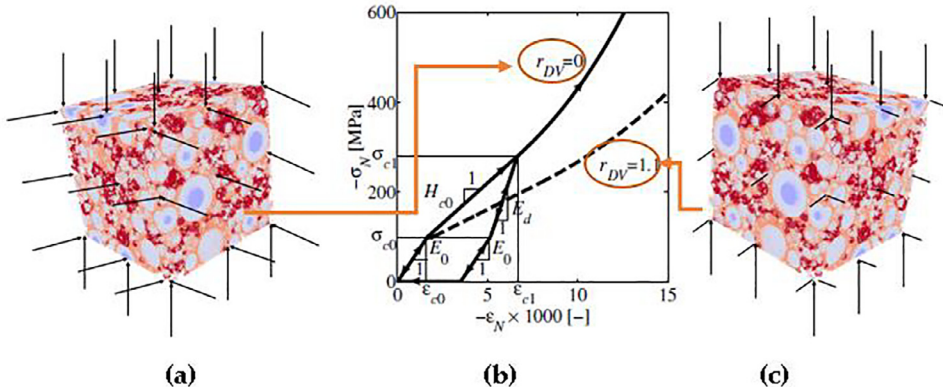


**Fig. 6.** (a) Hydrostatic numerical test (b) normal stress vs. normal strain curves in compression [22] (c) uniaxial confined numerical test.

$$-\varepsilon_N = \varepsilon_{c1} = k_{c0} \varepsilon_{c0} \quad (13)$$

where  $\varepsilon_{c0}$  is the normal strain at the initial peak point and  $\varepsilon_{c1}$  is the normal strain at the end of the linear hardening slope.

The material parameters ( $K_{c1}$  and  $K_{c2}$ ) were upscaled from a uniaxial confined simulation test on the cement paste scale, in which specimens were loaded under compression longitudinally, while transverse displacements were prevented. These parameters are evaluated in Eq. (14) [see [22]]

$$H_c(r_{DV}) = \frac{H_{c0}}{1 + k_{c2}(r_{DV} - k_{c1})} \quad (14)$$

where  $H_{c0}$  is the hardening Young's modulus from the hydrostatic simulation,  $H_c(r_{DV})$  is the hardening Young's modulus that considers the ratio of deviatoric-to-volumetric strain not equal to zero, and the brackets  $\langle \rangle$  are used in the Macaulay sense, i.e.,  $\langle x \rangle = \max(x, 0)$ . Choosing the uniaxial confined simulation test in which transverse expansion is prevented results in a constant deviatoric-to-volumetric strain ratio as well as permits use of Eq. (14).

**3.2.5.4. Friction parameters.** This group, characterized by three parameters (11–14) representing frictional effects at the facet region, requires future evaluation using the suggested methodology.

**3.2.5.5. Shear parameters.** This group is characterized by two parameters representing the interaction between shear and tensile behavior.  $n_t$  is the softening exponent, mainly governing nonlinear tensile and shear-tensile performance at the meso-level. To evaluate this parameter, further research is required.

(15)  $\sigma_s/\sigma_t$  is the shear-to-tensile strength ratio, where  $\sigma_s$  is the facet strength for pure shear and  $\sigma_t$  is the facet pure tensile strength (from Section 3.2.2).

In [21], the shear strength parameter was evaluated by performing a simulation test on the mortar-a4 scale under shear load. Shear behavior is a macroscopic response of the concrete/mortar-a4 scale calculated from the homogenization of the micro-scale response to macroscopic shear strain.

#### 4. Evaluating LDPM pore collapse under compaction parameters

The HYMOSTRUC3D is designed as an explicit 3D model to evaluate the chemical reaction of the hydrated cement paste intended for the microstructure of this scale. The specimen size allocated for this scale was  $100 \mu\text{m} \times 100 \mu\text{m} \times 100 \mu\text{m}$ ; more details on this choice and input parameters can be found in [21]. This model simulates the chemical reaction of the cement when mixed with water, providing information concerning the morphology, degree

of hydration, location, and expansion of particles. The microstructure, obtained from the HYMOSTRUC3D model together with the cement's mechanical properties, is then coupled with the Lattice model in order to indicate global mechanical behavior at the cement paste scale. This microstructure, initially presented in [21], was unchanged for the purposes of this research.

In the current study the lattice [17] material model was used to obtain the global compression properties of the cement paste at the age of 169 d under highly-confined conditions. It should be noted that this lattice model has been validated and verified experimentally [24]. In addition, the curing age of 169 d was chosen to represent the microstructure of cement paste because the uniaxial compression test for macroscopic validation was likewise performed at this age. For the purposes of the current research the local mechanical properties of lattice elements were the same as those presented in [21].

The microstructure of hydrated cement was first converted into a voxel-based digital image applied by the ImgLat lattice construction method [25]. Application of this method requires a choice of resolution length (mesh size), important because this length defines the intrinsic length of sub-microcracks nucleated by the rupture of a single link connecting two adjacent aggregates. Hence, this length is the intrinsic microstructure length, therefore must be selected in order to facilitate micromechanical analysis (mesh-independent) objectives. In this study the chosen resolution length was  $1 \mu\text{m}/\text{voxel}$ , in each of which a sub-voxel is created. A node that represents the disorder of the material is then randomly placed in each one of these sub-cells. Governing the amount of disorder in the material, the randomness range parameter value is between  $[0; 1]$ , where 1 represents the maximum expanse of disorder. In the current study the randomness parameter was set to 0.5, as recommended in [25]. The lattice structure is subsequently applied by connecting the neighbor's nodes with Timoshenko's beam elements. Mechanical properties were assigned for four different phases: un-hydrated cement, inner products, outer products, and CH. (Voids have no definition, so are not included in the lattice structure). Moreover, interface material properties were assigned to the layers between the phases. Therefore, the micro-scale model necessitated the input of nine different material properties, as presented in [21], which were calibrated to Portland cement concrete [25]. For each phase, input mechanical properties included the Young modulus, Shear modulus, Tensile strength, and Compression strength.

Two simulations, hydrostatic and uniaxial compression confined for lateral displacement, were completed at the cement paste scale to assess pore collapse and material compaction parameters for the LDPM. A hydrostatic simulation was performed by incrementally applying a displacement normal to all surfaces on the

specimen (see Fig. 5a). On those surfaces that were loaded (with incremental displacement), nodes were restrained against all rotation and displacement vector components. In other words, all nodes were free to fail in tension or compression. Cement paste unit cell size was  $100 \mu\text{m} \times 100 \mu\text{m} \times 100 \mu\text{m}$ , while the lattice network chosen for this simulation was quadrangular. The stress-strain curve obtained from the hydrostatic simulation was later used in evaluating four LDPM parameters (Fig. 7).

The initial peak value that can be observed in Fig. 6 is the yielding compressive stress,  $\sigma_{c0}$ . In addition, the unloading to normal modulus ratio  $E_d/E_0$  is generally presumed as equal to one, the initial hardening Young's modulus  $H_{c0}$  is obtained from the hardening slope, and the material parameter controlling the initial rehardening ( $k_{c0}$ ) is evaluated from  $k_{c0} = \varepsilon_{c1}/\varepsilon_{c0}$ , where  $\varepsilon_{c0}$  is the normal strain at the initial peak point and  $\varepsilon_{c1}$  is the normal strain at the end of the linear hardening slope.

The other two parameters ( $k_{c1}$  &  $k_{c2}$ ) are evaluated from the uniaxial compression confined to lateral displacement simulation performed by incrementally imposing a displacement normal to the longitudinal direction; transverse expansion was prevented by restraining all the displacement and rotation vectors on the appropriate surfaces (see Fig. 6c). On the surfaces loaded with incremental axial displacement components, nodes were restrained against rotations and displacements at the lateral directions. Furthermore, all nodes were free to fail in tension or compression. The lattice network chosen for the cement paste simulation was quadrangular, and unit cell size was  $100 \mu\text{m} \times 100 \mu\text{m} \times 100 \mu\text{m}$ . Simulated stress strain curves from both simulations are presented in Fig. 8.

$H_{c0}$  is the hardening Young's modulus from the hydrostatic simulation,  $H_c(r_{DV})$  is the hardening Young's modulus, which considers the ratio of deviatoric-to-volumetric strain that is not equal to zero, and the brackets  $\langle \rangle$  are used in the Macaulay sense, i.e.,  $\langle x \rangle = \max$

( $x, 0$ ). Choosing the uniaxial confined compression simulation results in a constant deviatoric-to-volumetric strain ratio thus permitting the use of Eq. (5).

For loading processes at constant  $r_{DV}$ , Eq. (15) is used:

$$r_{DV} = \frac{\varepsilon_N}{\varepsilon_V} - 1 \quad (15)$$

Volumetric strain is computed at the tetrahedron level from Eq. (16):

$$\varepsilon_V = \frac{(V - V_0)}{V_0} \quad (16)$$

where  $V$  is the current volume of the tetrahedron and  $V_0$  is the initial volume of the tetrahedron; current volume is computed by neglecting the effect of nodal rotation. The material parameter  $K_{c1}$  is assumed to be equal to 1.  $K_{c2}$  and is evaluated from Eq. (5), as shown in Fig. 8.

As previously mentioned, simulations on the cement paste scale were chosen to represent failure parameters due to pore collapse since only at this scale is porosity included. In other words, because the impact of the pore collapse phenomenon can be captured at the cement scale, it was chosen to represent the pore collapse and material compaction parameters. Under these conditions, we expect an initial peak value caused by the breakage of pore walls and the collapse of pores followed by a hardening due to their closure. Pore collapse is demonstrated in Fig. 9a by a visualization of these simulations, where the blue color represents the initial position, while the black represents the deformed position of elements, indicating pore collapse. In accordance with these same colors, Fig. 9b demonstrates the closure of pores at the hardening region. Note that deformed elements are presented with a scaling factor of 100.

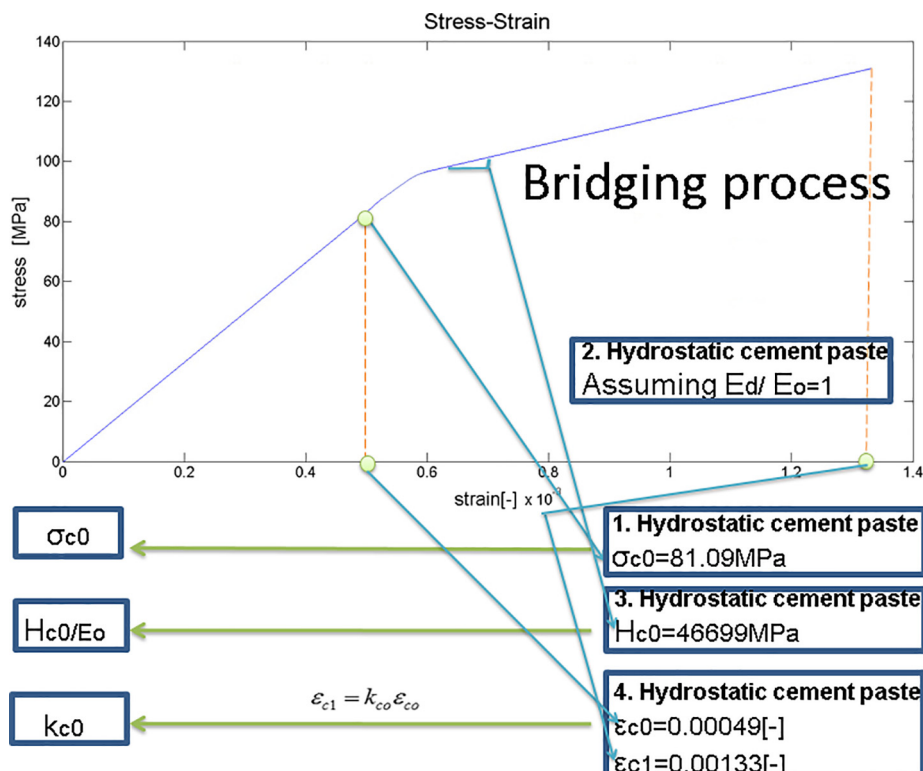
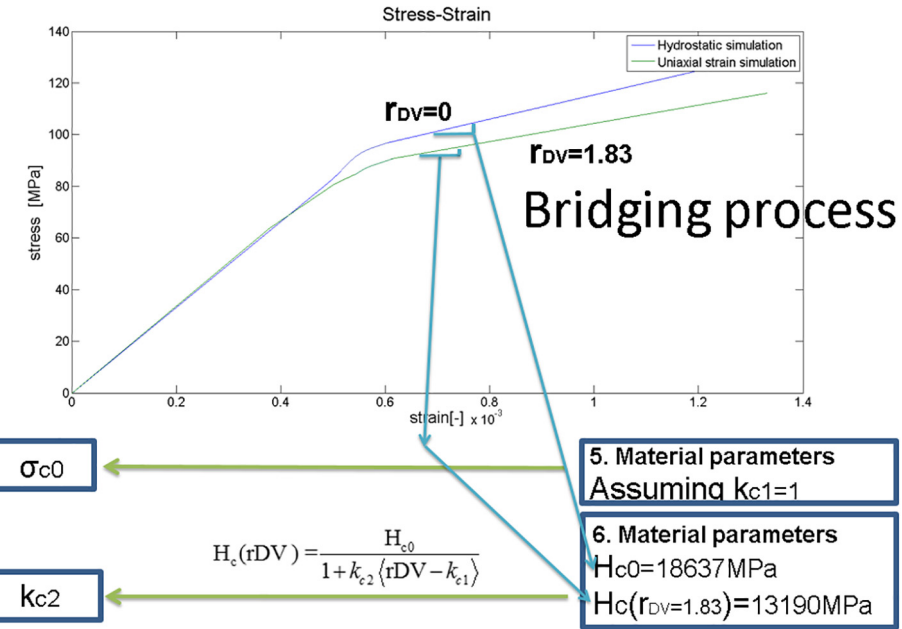
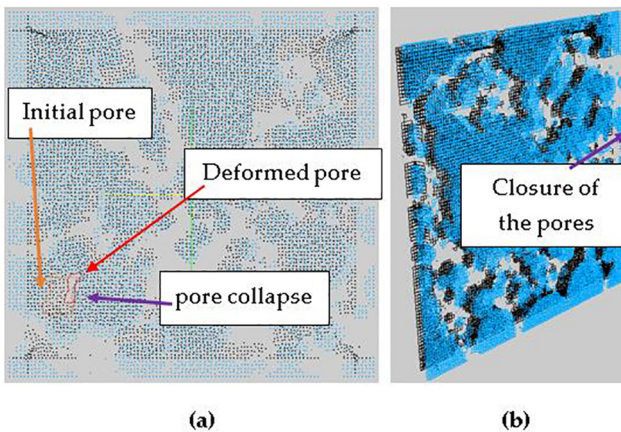


Fig. 7. Stress-strain curve of cement paste hydrostatic simulation.



**Fig. 8.** Stress–strain curves of hydrostatic and compression uniaxial confined to lateral displacement at cement paste scale.



**Fig. 9.** Initial (blue) and deformed (black) elements at cement paste scale representing a) pore collapse and b) pore closure. (For interpretation of the references to color in this figure legend, the reader is referred to the web version of this article.)

## 5. Results

### 5.1. Validation at cement paste scale

In this validation study the lattice model [17] was used to simulate pore collapse and material compaction parameters at the cement paste level. For this purpose, lattice simulation was compared to previously published experimental results [27] for a hardened Portland cement paste under uniaxial compression stress. To do so, a HYMOSTRUC3D simulation was performed on the same mix design though it is important to note here that the simulation was not performed on the same specimen size due to the limitations involving computational time, the cost of the HYMOSTRUC3D model, as well as the inability to conduct uniaxial confined experiments on a specimen that is too small.

The experiment published by [27] was conducted on specimens fitted into a cylindrical pressure vessel and loaded axially by a hard piston. The stiffness of the pressure vessel forces such a small lat-

eral expansion of specimens that the strain is almost uniaxial. The specimens were solid cylinders with a diameter of 0.02 m and a length of 0.04 m. The w/c ratio was 0.5, and a Portland cement Type I, meeting the ASTM C 150 specification, was used. The specimen size simulated on the HYMOSTRUC3D model to obtain the microstructure of cement was 100 μm × 100 μm × 100 μm. Finally, the microstructure generated for this mix design was used as an input for the lattice model.

This simulation was performed for a uniaxial confined test; transverse expansion was prevented by incrementally applying displacement normal to the longitudinal direction, and fixing all displacement and rotation on these surfaces (see Fig. 6c). On surfaces that were loaded (with incremental displacement), nodes were fixed against rotations and displacements in the lateral directions; all nodes were free to fail in tension or compression. The lattice unit cell size of the cement paste was 100 μm × 100 μm × 100 μm while the lattice network chosen for this simulation was quadrangular. The stress–strain for this lattice simulation result is presented in Fig. 10a and uniaxial experiment test results published in [27] are displayed in Fig. 10b.

As can be seen (Fig. 10) the values of  $\sigma_{co}$ ,  $H_{co}$  and  $\varepsilon_{co}$  are consistent with the results derived by the afore-mentioned experiment:

$$\sigma_{co,simulation} = 82.3195 \cong \sigma_{Experiment} = 12.45(\text{Ksi}) = 85.846(\text{MPa})$$

$$\begin{aligned} H_{co,simulation} &= 13036 \cong \sigma_{Experiment} = 1608.125(\text{Ksi}) \\ &= 11087.63(\text{MPa}) \end{aligned}$$

$$\varepsilon_{co,simulation} = 0.0008 \cong \varepsilon_{co,Experiment} = 0.001$$

We therefore conclude from this validation study that the lattice model is well-suited to represent the pore collapse and material compaction failure mods at the cement paste scale.

### 5.2. Validation at concrete scale

In order to validate our methodology, we performed uniaxial compression tests on three types of concrete specimens with a cross section of 100 mm × 100 mm [see also [28,29]]: two sets of specimens of 100 mm height with LF and HF boundary conditions

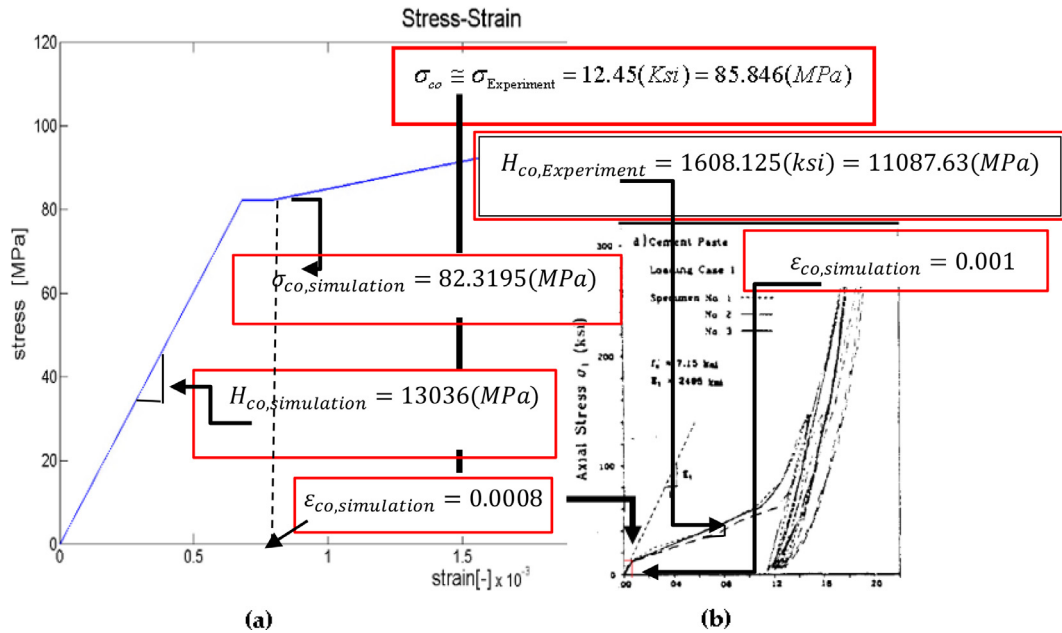


**Fig. 10.** a) Current study simulation, suitable for cement specification of [27] experiment b) uniaxial confined experimental test results [27]

and one set of specimens of 200 mm height with LF boundary conditions. These experimental results were then compared to LDPM simulations using the following parameters:

1. Using methodology innovated by [21], the Elastic, Fracture, and Shear parameters (**Table 2**) were evaluated based on the lower scale (i.e., cement, mortar-s, and mortar-a4) data, or, in other words, by using cement mineralogy composition, microscopic mechanical properties, as well as sand and aggregate mechanical properties.
2. Using the methodology presented in the current paper, Pore collapse under compaction parameters (**Table 3**) were evaluated based on cement paste scale data, i.e., using cement mineralogy composition and microscopic mechanical properties, as described in **Section 4**.
3. Friction and Shear interaction parameters (**Table 4**) were evaluated using calibration by curve-fitting between LDPM numerical results and macroscopic experimental results of the LF experiment with a height of 100 mm.

The simulation was performed using MARS software [30] that implements the LDPM. The MARS model, which includes two platens and the specimen of the 100 mm × 100 mm × 100 mm, is depicted in **Fig. 11**.

Boundary conditions that represent the friction between platens and specimen are governed by the sliding equation  $\mu s = \mu d + (\mu s - \mu d)s_0/(s_0 + s)$  [23] where the parameters suitable for the LF lubrication-type used in the experiment test were  $\mu s = 0.03$ ,  $\mu d = 0.0084$ ,  $s_0 = 0.0195$  mm. For the HF parameters were calibrated using the HF experimental results  $\mu s = 0.13$ ,  $\mu d = 0.015$ ,  $s_0 = 1.3$  mm.

The mix design parameters of meso-structures for the concrete scale are presented in **Table 1**; see also [28,29].

Five parameters were upscaled using the methodology proposed in [21] and as listed in **Table 2**.

While, six parameters were upscaled using the methodology presented in this paper (**Table 3**).

Likewise, four parameters were calibrated using the macroscopic experimental results of the LF experiment with a height of 100 mm, as presented in **Table 4**.

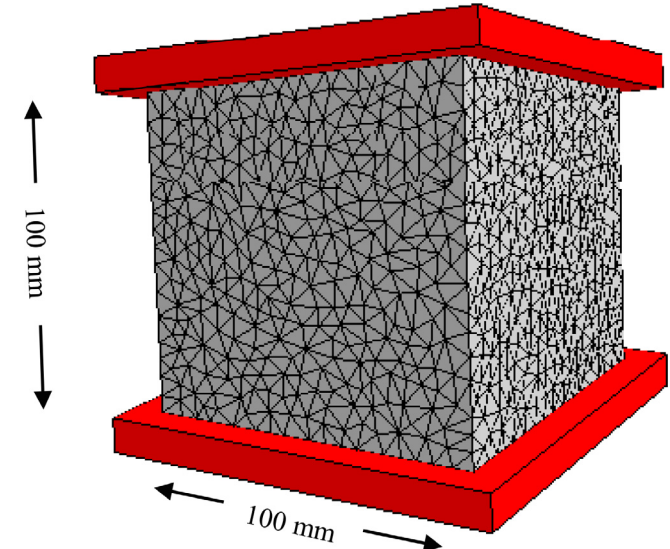


**Fig. 11.** MARS specimen model.

**Table 1**  
LDPM mix-design parameters.

Symbol	C[Kg/m <sup>3</sup> ]	w/c [-]	a/c [-]	do[mm]	da[mm]	Nf[-]
Sec.	391	0.567	2.2532	4	14	0.425

**Table 2**  
Elastic, fracture, and shear parameters [21]

	Up-scaled
E <sub>0</sub> [MPa]	30,150
$\alpha[-]$	0.35
$\sigma_t$ [MPa]	4,259
G <sub>t</sub> = L <sub>t</sub> $\sigma_t^2$ /2E <sub>0</sub> N/m	29,62
$\sigma_s/\sigma_t[-]$	2.63

**Table 3**  
Upscaled compression parameters.

	Up-scaled
$\sigma_{co}$ [MPa]	81.09
$H_{co}/E_0[-]$	0.35
$Hd/E_0[-]$	1
$K_{c0}[-]$	2.72
$K_{c1}[-]$	1
$K_{c2}[-]$	0.4975

**Table 4**  
Friction and Interaction parameters.

	Calibrated
$n_t[-]$	0.5
$\mu_0[-]$	0.2
$\mu_\infty[-]$	0
$\sigma_{No}[-]$	600

Use of the above-mentioned LDPM parameters and experimental results for the different types of specimens and boundary conditions are presented in Fig. 12. Right curves show the average longitudinal strain versus the longitudinal average stress, while the left curves show the average transverse strain versus the average longitudinal stress. LF 100 mm were used to calibrate the parameters shown in Table 4; excellent correlation with experimental results was found. Moreover, the HF 100 mm used to calibrate the sliding parameters between platens and specimen also showed excellent agreement with experimental results. Finally, the LF 200 mm used for validation, i.e., the parameters seen in Tables 2–4, likewise showed excellent agreement with experimental results, including the post-peak response of lateral and longitudinal directions. It is important to note that validated results were found to be almost identical for the peak value and for the inclination on the curves of the longitudinal and lateral directions.

That the difference between the experimental and the suggested methods is negligible leads us to conclude that the suggested upscale formulation is appropriate for use in evaluating LDPM parameters based on microscopic properties at the lower scales. Furthermore, validation by simulating different specimen sizes showed a consistently excellent fit, thereby demonstrating

that compressive parameters can be derived from the cement paste scale. Finally, validation also showed that the LDPM can capture the size effect. However, although HF boundary condition parameters were calibrated, they remain to be validated; this objective, requiring an additional set of experiments from the same batch, will be fulfilled in future research.

## 6. Case study involving different mixtures, and unit cell boundaries for LDPM parameters and macroscopic validation

A HYMOSTRUC3D simulation was performed for the same concrete mix [31], as the one utilized for the triaxial compression test in macroscopic validation. The size of  $100 \mu\text{m} \times 100 \mu\text{m} \times 100 \mu\text{m}$  was simulated; see Table 5 for specification details. Geometrical structure of this cement paste at the age of 85 h is shown in Fig. 13. This particular age was chosen for the sake of comparison to experimental results for the same age.

### 6.1. Evaluation of mechanical properties of cement paste

As previously stipulated, the lattice model [32] was simulated for the cement paste at the age of 85 d. It requires input parameters such as the mechanical properties of each solid layer as shown in Table 2, while the addition of a layer of fly ash is included in Table 6. At this scale two homogenization steps were applied:

1. This step is similar to that presented in Section 3.2 [21], though here it was performed on the case study.

**Table 5**  
Cement specifications for HYMOSTRUC3D.

Characteristic	Inputs Specification
w/c	0.57
Mineralogical composition of clinker and gypsum in cement (85%)	C3S: 62, C2S: 13, C3A: 7, C4AF: 2.4
Minimum particle diameter and cement fineness (Rosin-Rammler distribution)	1 $\mu\text{m}$ $n = 1.54503, b = 0.01018$
Chemical composition of fly ash (15%)	$\text{Al}_2\text{O}_3: 25.8, \text{SiO}_2: 54.9, \text{MgO}: 1.8, \text{CaO}: 8.7, \text{Fe}_2\text{O}_3: 6.9, \text{SO}_3: 0.6, \text{Na}_2\text{O}: 0.3, \text{K}_2\text{O}: 0.3$
Curing temperature	20 °C

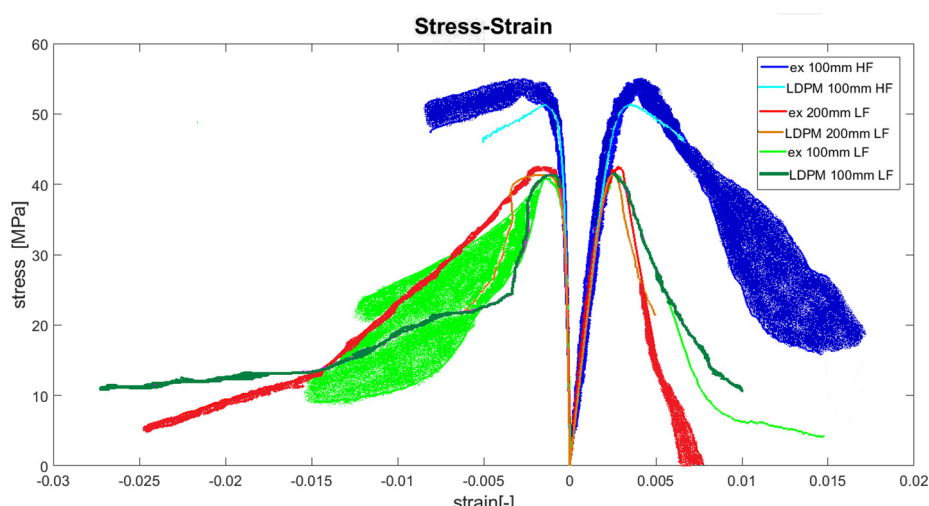


**Fig. 12.** Uniaxial compression test experimental results with LF 100 mm (light green curve), LDPM results with LF 100 mm (green curve), experimental results with LF 200 mm (red curve), LDPM results with LF 200 mm (orange curve), experimental results with HF 100 mm (blue curve) and LDPM results with HF 100 mm (light blue curve). (For interpretation of the references to color in this figure legend, the reader is referred to the web version of this article.)

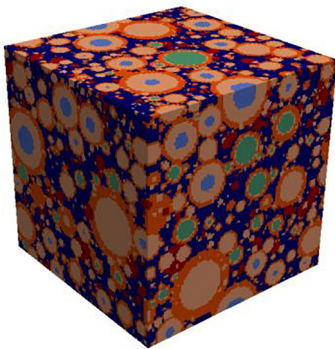


**Fig. 13.** Simulated microstructures of cement paste for specimen size  $100 \mu\text{m} \times 100 \mu\text{m} \times 100 \mu\text{m}$  at 85 d (dark blue is porous cement, bright blue is unhydrated cement, bright orange is inner hydration product, dark orange is outer hydration product, green is fly ash, and red is CH-calcium hydroxides). (For interpretation of the references to color in this figure legend, the reader is referred to the web version of this article.)

- This step is similar to that presented in Section 3.2 [21], though here it was performed on the case study. The homogenized mechanical properties of cement paste were evaluated for input parameters of the matrix at the mortar-s scale (see Fig. 14).

## 6.2. Upscaling the mortar-s scale

Reference to Section 3.3 from Sherzer et al. (2017) was made for the current case study, though specimen size chosen for these purposes was  $3 \text{ mm} \times 3 \text{ mm} \times 3 \text{ mm}$  and resolution was  $0.1 \text{ mm}/\text{voxel}$ . The mortar-s geometrical structure, achieved by Anm material model, was used to obtain the input parameters for the matrix at this scale, as presented in Tables 7 and 8.

**Table 6**

Specifications of lattice's additional layer of fly ash.

No.	Element Type	Young Modulus E (GPa)	Shear Modulus G (GPa)	Tensile Strength $f_t$ (GPa)	Compression Strength $f_c$ (GPa)
1	Fly ash	120	48	1.8	-18
2	Interface -Unhydrated Cement and Fly ash	127	50.824	1.8	-18
3	Interface-Inner and Fly ash	48	19.2	0.24	-2.4
4	Interface-Outer and Fly ash	37.18	14.872	0.15	-1.5
5	Interface- (CH)- and Fly ash	51.76	20.7	0.264	-2.64
6	Interface-Unhydrated and Outer	38	15.2	0.15	-1.5
9	Interface-Inner and CH	31.5	12.6	0.24	-2.4

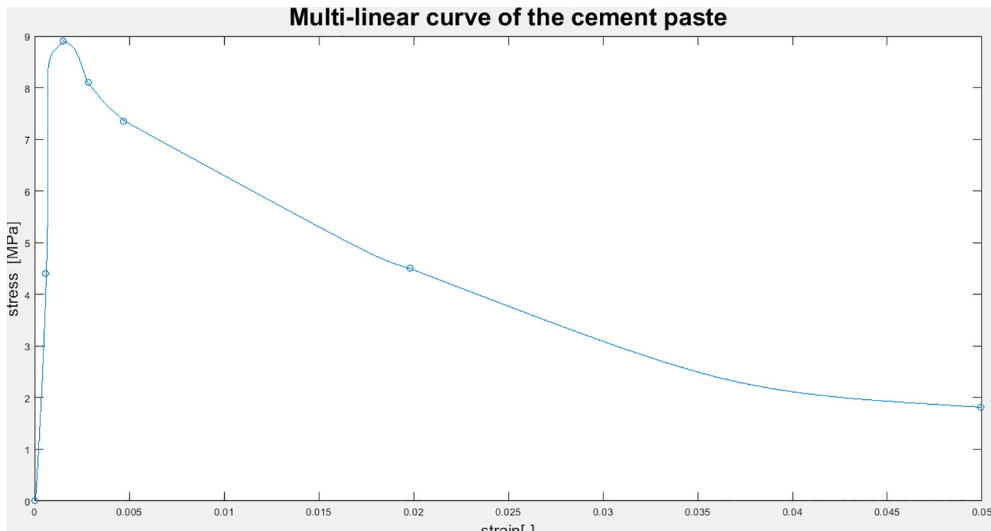


**Fig. 14.** Simulated stress-strain curve for the cement paste obtained from tensile test.

**Table 7**

Mortar-s Anm model input parameters.

Input Category	Input Specification
Specimen size ( $\text{mm}^3$ )	$3 \times 3 \times 3$
Sand mass (g)	0.285
Sand density ( $\text{g}/\text{mm}^3$ )	0.00265

**Table 8**

Sieve distribution at mortar-s scale.

Input Category	Input Specification
Sieve distribution (mm)	1.2–0.5
Mass percentage (%)	100

Subsequently, the lattice model was used to simulate the mechanical properties at the mortar-s scale (see Fig. 15). The mechanical parameters for the cement paste is presented in Fig. 14, while the sand as well as interface properties are presented in Sherzer et al. (2017); see also [33].

## 6.3. Upscaling the mortar-a4.75 scale

Reference for this section (with the exception of maximum aggregate size) was made to Sherzer et al. (2017) in order to examine the different boundary conditions existing between the lattice model and the LDPM. Here, as the maximum aggregate size is 4.75, the size scale was chosen to be  $12 \text{ mm} \times 12 \text{ mm} \times 12 \text{ mm}$ , while resolution was chosen to be  $1 \text{ mm}/\text{Voxel}$ . Specifications for the Anm model are presented in Table 9.

Mechanical parameters of the mortar-a4.75 scale were achieved by the lattice model [32] simulation, while mortar-s mechanical properties were achieved from the previous scale simulation (see

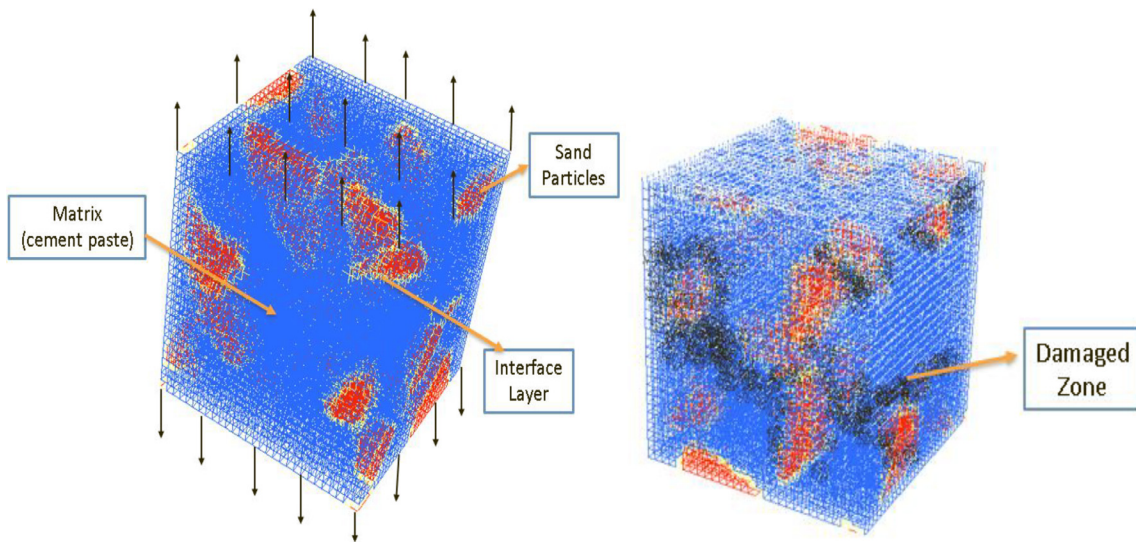


**Fig. 15.** (a) Uniaxial tension analysis of mortar-s scale (cement paste in blue, sand particles in red, interface layer in white) (b) resulting damaged zone (underlined in black) on mortar-s scale. (For interpretation of the references to color in this figure legend, the reader is referred to the web version of this article.)

**Table 9**  
Mortar-a4 specifications for Anm model.

Input category	Input specification
Specimen size (mm <sup>3</sup> )	12 × 12 × 12
Aggregate mass (g)	0.5058
Aggregate density (g/mm <sup>3</sup> )	0.00265
Aggregate size distribution (mm)	1.2–4.75
Mass percentage of distribution (%)	100

**Fig. 16**) and the aggregates and interface between aggregate mechanical properties were identical to those in Sherzer et al. (2017).

#### 6.4. Elastic, fracture, and shear parameters obtained for case study

This section presents evaluation of the elastic ( $E_0, \nu$ ), fracture ( $l_t, \sigma_t$ ), and shear

( $\sigma_t/\sigma_t$ ) parameters needed for LDPM simulation. Uniaxial tensile and pure shear tests were performed using the lattice model. Simulations were repeated from sec. 4.5 for the case study; see Fig. 17 for the crack pattern of this scale and the geometrical structure for tensile simulation.

The resulting stress-strain curve evaluating the fracture parameters is presented in Fig. 18.

After conducting a tensile simulation, we performed a shear simulation shear simulation. The results of this simulations are shown in Fig. 19 and represent the shear stress–shear strain, deformed elements, and crack pattern.

#### 6.5. Evaluating pore collapse under compaction parameters

Evaluation of pore collapse was repeated for this case study. As presented in Fig. 20, the stress-strain curve obtained from

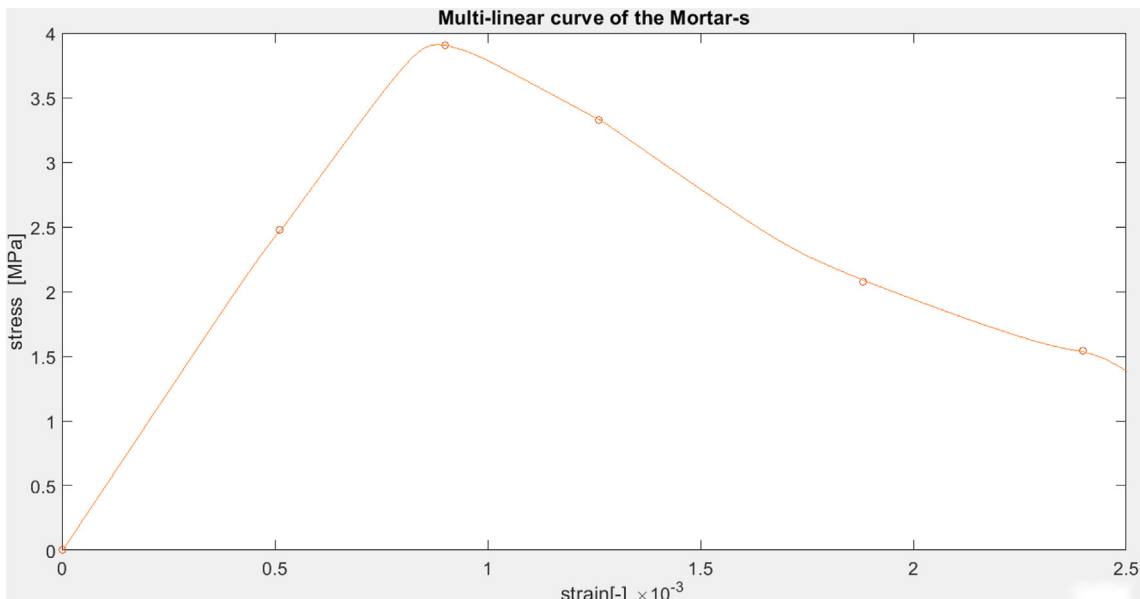


**Fig. 16.** Mortar-s stress–strain curve.

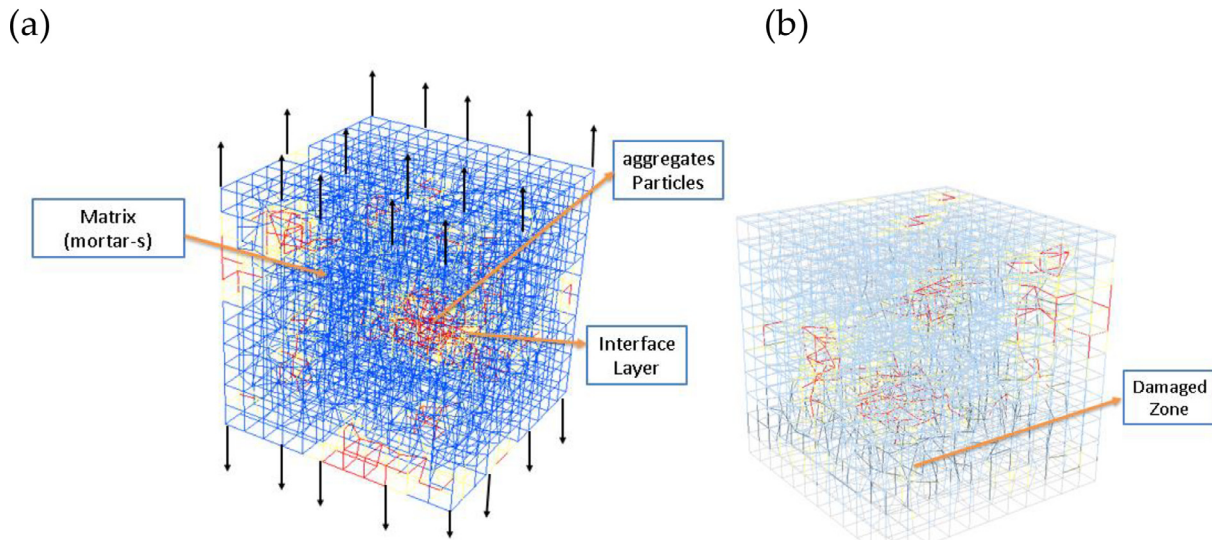


**Fig. 17.** (a) mortar-a4.75 geometrical structure for tensile simulation (mortar-s in blue, aggregate particles in red, and interface layer in yellow) (b) damaged zone (in black) for current simulation. (For interpretation of the references to color in this figure legend, the reader is referred to the web version of this article.)

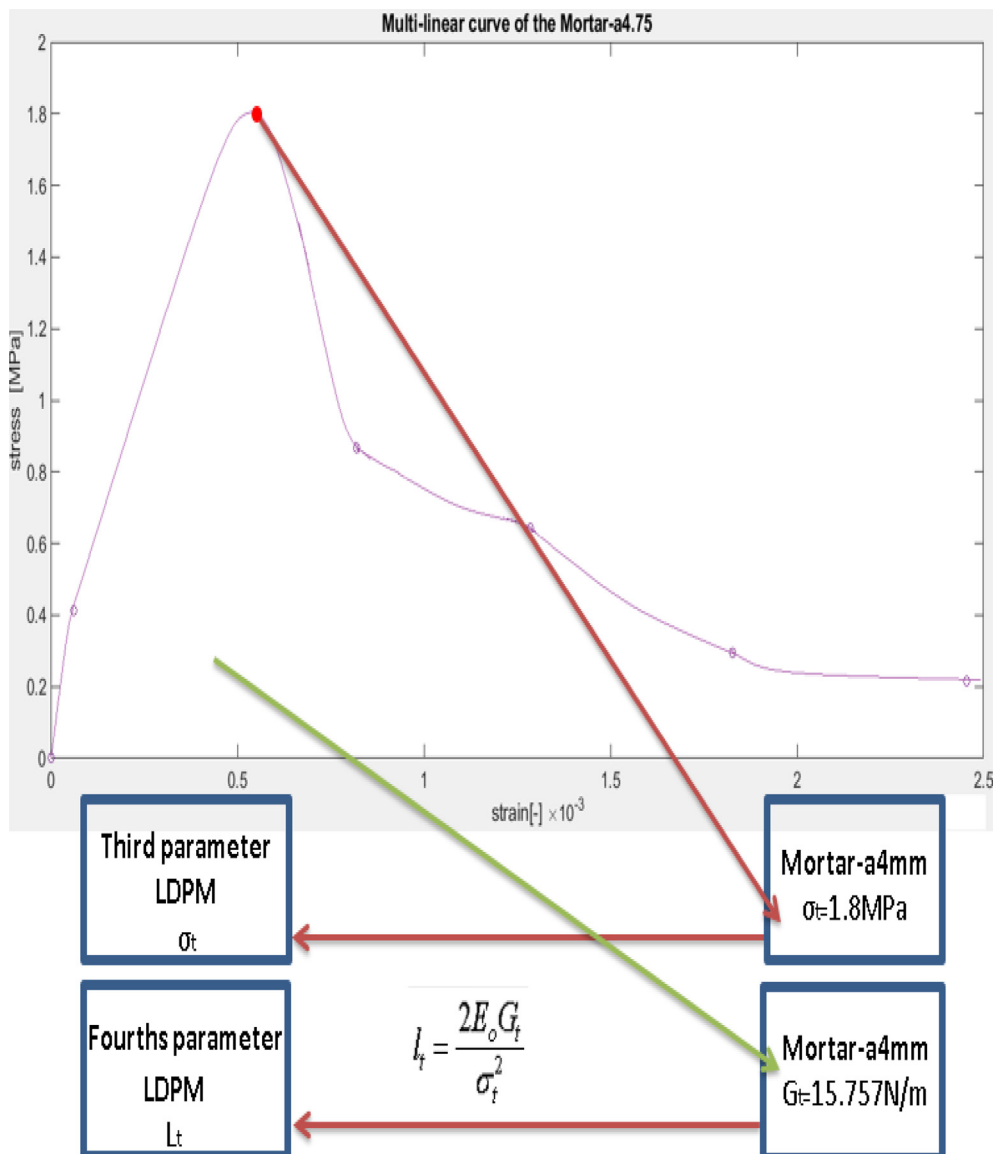


**Fig. 18.** Simulated stress-strain curve for mortar-a4 scale obtained from tensile test.

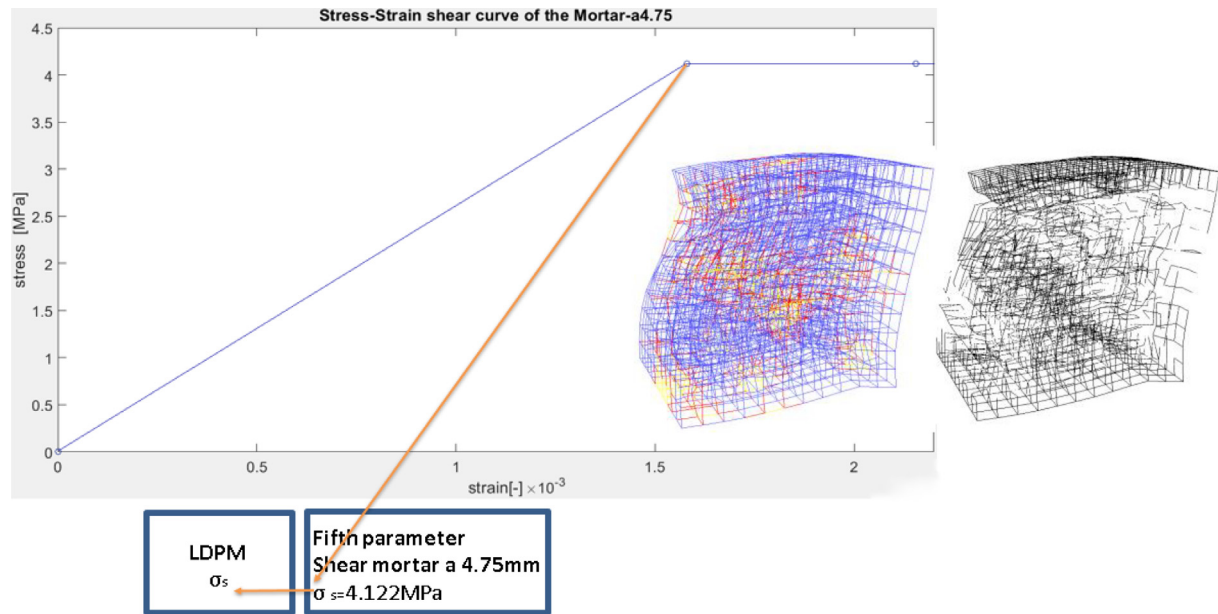


Fig. 19. Shear stress–shear strain curve, shear deformed mode and damaged elements (in black).

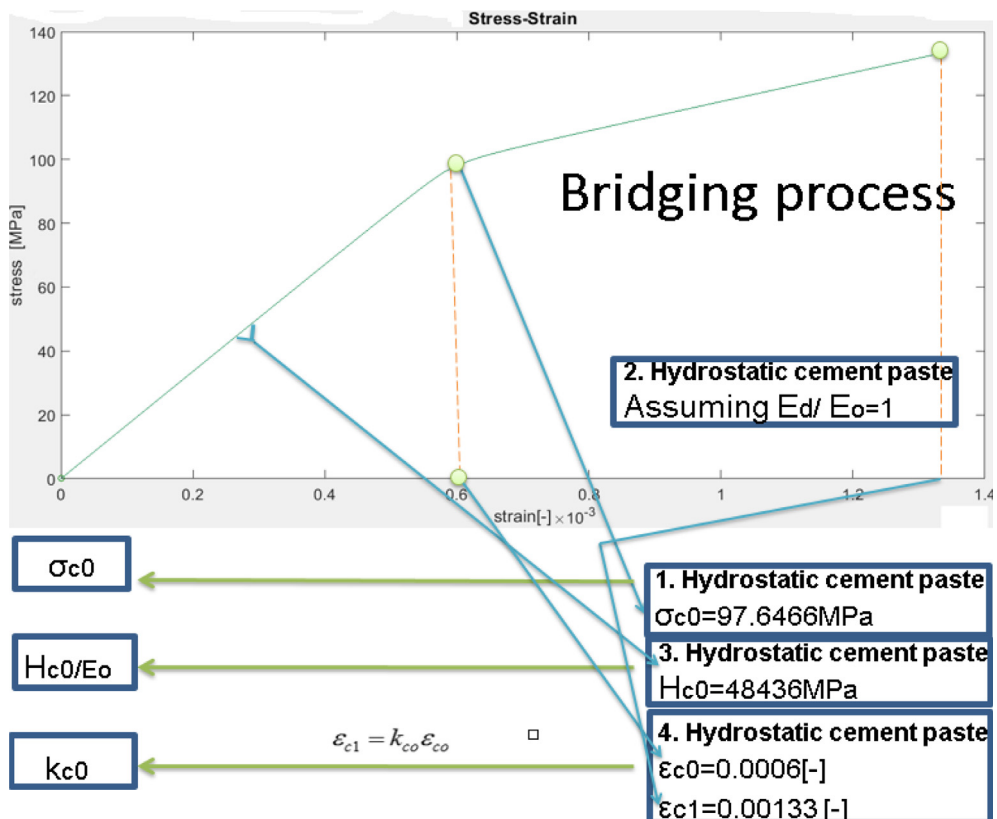


Fig. 20. Stress–strain curves of hydrostatic and compression uniaxial confined to lateral displacement at cement paste scale.

hydrostatic and confined compression simulations were used to evaluate six LDPM parameters.

#### 6.6. Validation for case study at the concrete scale

In this section triaxial compressive tests were done in order to validate the case study. Validation was performed to examine the capabilities of the upscaling methodology for predicting confine-

ment effect as well as to examine different, arbitrary (i.e., maximum aggregate size) for coupling between the mortar and concrete scales. Triaxial compressive tests were exposed to a hydrostatic pressure up to a target confining pressure; at that point, the lateral pressure remained constant on cylindrical surfaces, while longitudinal surfaces continued to be loaded. Next, calibrated LDPM mechanical parameters were achieved using two methods. First, LDPM material parameter calibration was based

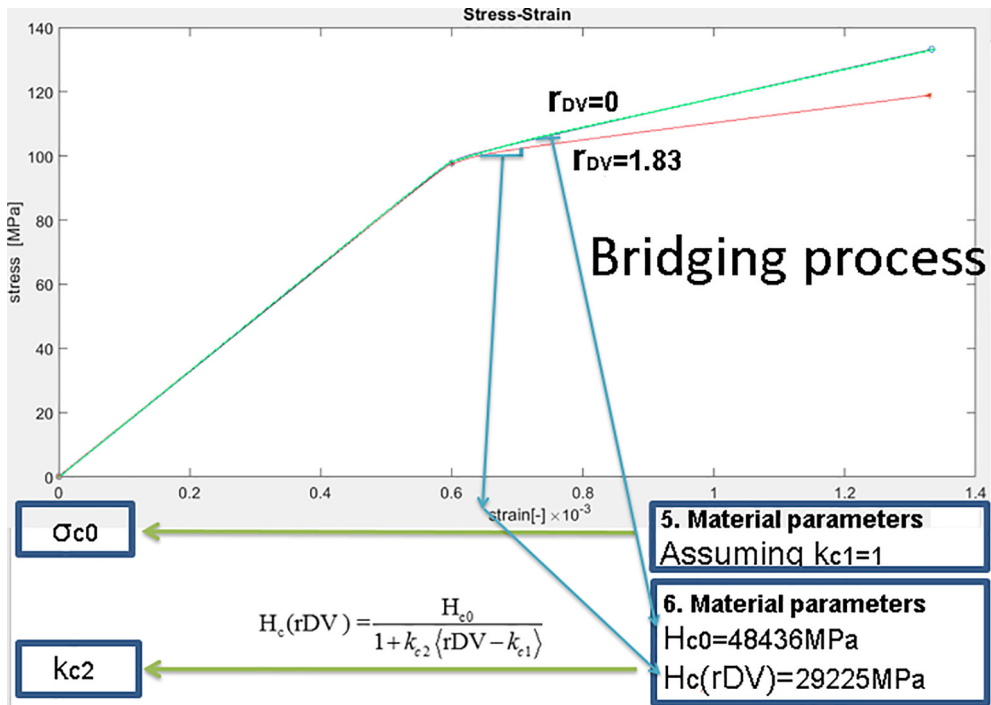


Fig. 20 (continued)

on experimental data [31] relevant to triaxial experiments with a confining pressure of  $p = 20$  MPa and 200 MPa, then compared to LDPM numerical simulations performed in [23]. The defined material parameters for this calibration process is presented in (Table 10, see also [23]). A second method of evaluating elastic, fracture, shear, and pore collapse parameters was done with the proposed upscaling methodology, while remaining LDPM parameters were estimated with a curve-fitting procedure for  $p = 100$  MPa (see Table 11). Our validation processes were achieved by simulating with other variable confinement presses ( $p = 200$  and 400) without changing the material parameters for each of these methods. It is also important to note that, in previous research that compared validation processes for these simulations to experimental results, excellent correlation was demonstrated [23]. In this study macroscopic experiments were performed on cylindrical specimens having a longitudinal dimension of 101.6 mm (4 in) and a diameter of 25.4 mm (1 in); mix design is reported in Table 12. Boundary conditions were high-friction, the effects of which are

**Table 11**  
Parameters of second method.

	Upscaled
$E_0[\text{MPa}]$	38,636
$\alpha[-]$	0.25
$\sigma_t[\text{MPa}]$	1.8
$L_t[\text{mm}]$	375.62
$\sigma_s/\sigma_t[-]$	2.29
$n_t[-]$	0.2
$\sigma_{co}[\text{MPa}]$	97.6466
$H_{co}/E_0[-]$	1.254
$k_{col}[-]$	2.22167
$k_{c1}[-]$	1
$k_{c2}[-]$	0.29588
$\mu_0[-]$	0.07
$\mu_\infty[-]$	0.007
$\sigma_{No}[\text{MPa}]$	600
$E_d/E_0[-]$	1.81

**Table 12**  
Parameters of LDPM mix-design.

Symbol	$C[\text{Kg/m}^3]$	$w/c [-]$	$a/c [-]$	$do[\text{mm}]$	$da[\text{mm}]$	$Nf[-]$
Sec.	264	0.553	7.1	4.75	9.5	0.5

contained within the LDPM by a slading equation [22,23], while the input parameters for this equation are ( $\mu_s = 0.12$ ,  $\mu_d = 0.015$ ,  $s_0 = 0.5$  mm).

The triaxial compressive simulations are presented in Fig. 21, in which the blue, yellow, and green curves represent the first method (see also [23]), and the red, purple, and light blue curves represent the second proposed method.

Fig. 21 compares the two methods described above. Using our proposed methodology, we not only achieved a perfect match for the calibration process but validation at 200 Mpa confinement also showed great fit. Likewise, results for the 400 Mpa confinement up

**Table 10**  
Parameters of first method.

	Macroscopic calibration
$E_0[\text{MPa}]$	38,636
$\alpha[-]$	0.25
$\sigma_t[\text{MPa}]$	4.16
$L_t[\text{mm}]$	100
$\sigma_s/\sigma_t[-]$	2.7
$n_t[-]$	0.2
$\sigma_{co}[\text{MPa}]$	120
$H_{co}/E_0[-]$	0.67
$k_{col}[-]$	3.8
$k_{c1}[-]$	1.2
$k_{c2}[-]$	5
$\mu_0[-]$	0.4
$\mu_\infty[-]$	0
$\sigma_{No}[\text{MPa}]$	600
$E_d/E_0[-]$	1.81

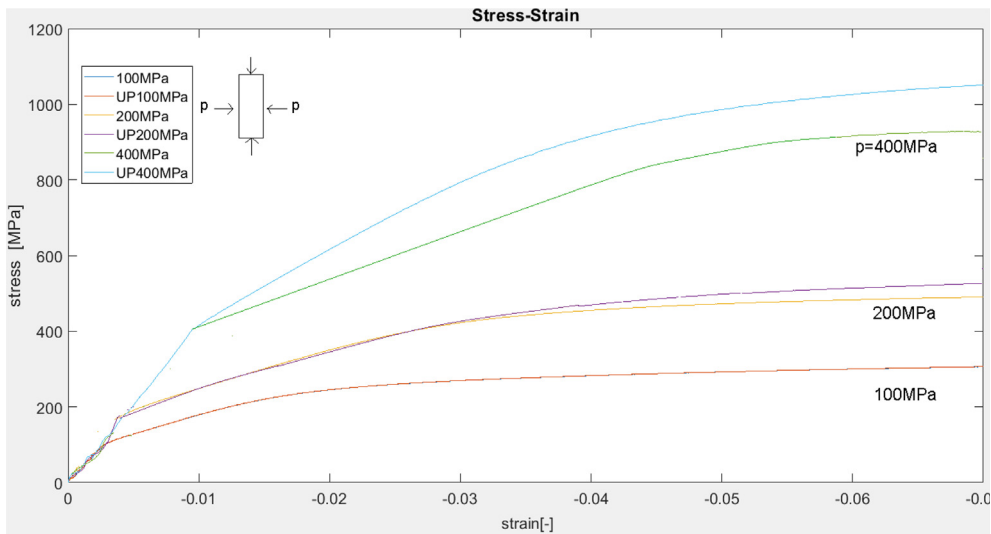


**Fig. 21.** Triaxial compression simulations using two different methods under variable confinement pressures ( $p = 100, 200$  and  $400$  MPa).

to the initial peak point were remarkable, yet after this region they indicate poorer adjustment.

Finally, we have determined conclusively that our methodology is well-suited for different (i.e., maximum aggregate size for mortar scale) for coupling between the mortar and concrete scales. Having chosen for the purposes of this case study the maximum aggregate size for mortar scale of 4.75 mm, we have thus demonstrated that method type is arbitrary.

## 7. Conclusion

This paper presents a multi-scale, upscaling methodology based on upscaling cement paste pore collapse response for evaluating LDPM compressive parameters. Evaluation of compressive mechanical LDPM parameters from lower-scale models requires performing simulation at the cement paste level under different load combinations. To this end, simulations were performed to evaluate the pore collapse and material compaction parameters needed for the LDPM. Choices of simulations were made in order to characterize failure mode as a function of pore collapse since, in the proposed method, porosity features are included only at the cement paste scale. We expected an initial peak value (decrease of slope) caused by the breakage of pore walls and collapse of pores, followed by a hardening behavior as a result of pore closure.

A validation study was performed on two of the simulated scales. At the cement paste scale the numerical value from the simulation fit well with experimental results. At the concrete scale the LF 200 mm proved to fit very well with experimental results. In addition, validation was undertaken in order to corroborate the proposed upscaling method with different concrete mix, different maximum aggregate size for coupling between mortar and concrete scales, and different tests under variable confining pressures. Even after changing these conditions, we achieved an excellent match between experimental results and simulations, therefore our method can be considered as arbitrary.

Accurate application of this method will reduce the need for calibration with experimental results. Furthermore, its implementation will enable predicting behavior of a concrete structure based on evaluation at different scales of its components.

A more comprehensive validation study that would include experiments on a wider range of scales is recommended.

## Declaration of Competing Interest

The authors declare that they have no known competing financial interests or personal relationships that could have appeared to influence the work reported in this paper.

## Acknowledgments

This research was supported by the Israel Ministry of Science, Technology and Space, Government of Israel, COST Action TU1404, and Nesher-Israel Cement Enterprises.

## References

- [1] A. Fascatelli, J.E. Bolander, N. Nisticó, Lattice discrete particle modeling of concrete under compressive loading: multiscale experimental approach for parameter determination, *J. Eng. Mech.* 144 (8) (2018) 04018058.
- [2] G.G. Balmer, Shearing Strength of Concrete Under High Triaxial Stress-computation of Mohr's Envelope as a Curve, Branch of Design and Construction, US Bureau of Reclamation1949.
- [3] M.D. Kotsovos, J.B. Newman, Generalized stress-strain relations for concrete, *J. Eng. Mech. Div.* 104 (4) (1978) 845–856.
- [4] J. Newman, *Concrete under Complex Stress*, Lydon, FD, Developments in Concrete Technology-1, Applied Science Publishers, London, 1979.
- [5] J.G. van Mier, *Fracture of Concrete Under Complex Stress*, Faculty of Civil Engineering, Delft University of Technology, 1986.
- [6] W. Chuan-Zhi, G. Zhen-Hai, Z. Xiu-Qin, Experimental investigation of biaxial and triaxial compressive concrete strength, *Mater. J.* 84 (2) (1987) 92–100.
- [7] S.S. Smith, K.J. Willam, K.H. Gerstle, S. Sture, Concrete over the top-or, is there life after peak?, *Mater. J.* 86 (5) (1989) 491–497.
- [8] R. Bellotti, P. Rossi, Cylinder tests: experimental technique and results, *Mater. Struct.* 24 (1) (1991) 45–51.
- [9] K.K. Dahl, A failure criterion for normal and high strength concrete, *Lynby* (1992).
- [10] I. Imran, S. Pantazopoulou, Experimental study of plain concrete under triaxial stress, *ACI Mater. J.-Am. Concr. Inst.* 93 (6) (1996) 589–601.
- [11] Q. Li, F. Ansari, Mechanics of damage and constitutive relationships for high-strength concrete in triaxial compression, *J. Eng. Mech.* 125 (1) (1999) 1–10.
- [12] C. Poinard, Y. Malecot, L. Daudeville, Damage of concrete in a very high stress state: experimental investigation, *Mater. Struct.* 43 (1–2) (2010) 15–29.
- [13] X.H. Vu, Y. Malecot, L. Daudeville, E. Buzaud, Effect of the water/cement ratio on concrete behavior under extreme loading, *Int. J. Numer. Anal. Meth. Geomech.* 33 (17) (2009) 1867–1888.
- [14] R. Marino, Strength and ductility of confined high strength concrete, *Earthquake Engineer 10th World* 5 (1992) 2609.
- [15] G. Ye, K. Van Breugel, A. Fraaij, Three-dimensional microstructure analysis of numerically simulated cementitious materials, *Cem. Concr. Res.* 33 (2) (2003) 215–222.
- [16] K. Van Breugel, Numerical simulation of hydration and microstructural development in hardening cement-based materials (I) theory, *Cem. Concr. Res.* 25 (2) (1995) 319–331.

- [17] Z. Qian, E. Schlangen, G. Ye, K. Van Breugel, Multiscale lattice fracture model for cement-based materials, ICCM (2012).
- [18] A. Naija, K. Miled, O. Limam, A discrete micromechanical model for predicting HSC compressive strength based on a yield design approach, *Constr. Build. Mater.* 175 (2018) 714–725.
- [19] D. Markovic, A. Ibrahimbegovic, On micro-macro interface conditions for micro scale based FEM for inelastic behavior of heterogeneous materials, *Comput. Methods Appl. Mech. Eng.* 193 (48–51) (2004) 5503–5523.
- [20] Z. Qian, E. Garboczi, G. Ye, E. Schlangen, Annm: a geometrical model for the composite structure of mortar and concrete using real-shape particles, *Mater. Struct.* 49 (1–2) (2016) 149–158.
- [21] G. Sherzer, P. Gao, E. Schlangen, G. Ye, E. Gal, Upscaling cement paste microstructure to obtain the fracture, shear, and elastic concrete mechanical LDPM parameters, *Materials* 10 (3) (2017) 242.
- [22] G. Cusatis, D. Pelessone, A. Mencarelli, Lattice discrete particle model (LDPM) for failure behavior of concrete. I: theory, *Cem. Concr. Compos.* 33 (9) (2011) 881–890.
- [23] G. Cusatis, A. Mencarelli, D. Pelessone, J. Baylot, Lattice Discrete Particle Model (LDPM) for failure behavior of concrete. II: calibration and validation, *Cem. Concr. Compos.* 33 (9) (2011) 891–905.
- [24] E. Schlangen, J. Van Mier, Experimental and numerical analysis of micromechanisms of fracture of cement-based composites, *Cem. Concr. Compos.* 14 (2) (1992) 105–118.
- [25] Z. Qian, Multiscale modeling of fracture processes in cementitious materials, Microlab, Section of Materials and Environment, Faculty of Engineering and Geoscience, Delft University of Technology, 2012.
- [26] Z.P. Bažant, G. Pijaudier-Cabot, Measurement of characteristic length of nonlocal continuum, *J. Eng. Mech.* 115 (4) (1989) 755–767.
- [27] Z.P. Bazant, F.C. Bishop, T.-P. Chang, Confined compression tests of cement paste and concrete up to 300 ksi, *ACI J.* 33 (1986) 553–560.
- [28] G. Sherzer, Development, Calibration & Validation of Lateral Displacement for Concrete Uniaxial Compression Test, Structural Engineering, Ben-Gurion University, 2014.
- [29] G. Sherzer, E. Marianchik, R. Cohen, E. Gal, Development, Calibration & Validation of Lateral Displacement for Concrete Uniaxial Compression Test, presented at the CONCREEP 10, Vienna University of Technology, Austria, 2015, pp. 1420–1429.
- [30] D. Pelessone, MARS, modeling and analysis of the response of structures—users manual, ES3, Inc. San Diego, CA, USA (2006).
- [31] Z.P. Bažant, Y. Xiang, M.D. Adley, P.C. Prat, S.A. Akers, Microplane model for concrete: II: data delocalization and verification, *J. Eng. Mech.* 122 (3) (1996) 255–262.
- [32] Z. Qian, E. Schlangen, G. Ye, K. Van Breugel, Multiscale lattice fracture model for cement-based materials, ICCM 2012: 4th International Conference on Computational Methods, ICCM, Gold Coast, Australia, 2012, pp. 25–28.
- [33] Z. Qian, Multiscale modeling of fracture processes in cementitious materials, Delft University of Technology, TU Delft, 2012.